Practical Issues Related to the Interferometric Imaging of Geosats

H. R. Schmitt[a], S. R. Restaino[a], D. Mozurkewich[b], J. E. Mason[c], K. R. Bock[c], J. A. Dank[c], J. T. Armstrong[a], E. K. Baines[a], G. Feller[c]

[a]Remote Sensing Division, Naval Research Laboratory, Washington, DC 20375, USA;
[b]Seabrook Engineering, Seabrook, MD 20706, USA
[c]Lockheed Martin Advanced Technology Center, CA 94306 ,USA

ABSTRACT

Imaging geostationary satellites from the ground is an important Space Situational Awareness diagnostic tool that will require the use of optical interferometry. We developed a series of imaging and data quality simulations that allow us to investigate issues related to the interferometric imaging of such targets. We discuss the number of baselines and sampling density needed to achieve different resolutions. We investigate the effect of target size relative to the resolving power of a single telescope in the interferometer, and how this influences the amount of light coupled into a fiber and the observed interferometric visibility amplitude. We also investigate a method that will allow one to determine and correct phase variations due to different delay sources in a post-processing way. The results presented here will be important to guide the design of future optical interferometers dedicated to the imaging of geosats.

Keywords: geostationary satellites, optical interferometry imaging, telescope arrays

1. INTRODUCTION

A critical gap in the Space Situational Awareness capability is the ability to image objects in geostationary orbits from the ground, for the purposes of identification and characterization. Obtaining a high-resolution image of an object at a these altitudes (37,000 km) is a challenging endevour. An object with a dimension of 10 m corresponds to an angle of 0.27μrad (55 milli arcsec), equivalent to the resolving power of a 3.6 m telescope observing at 800 nm. In order to obtain high-resolution ($\sim$10 cm) ground based images of these target will require the use of optical interferometry.

Over the last years our group has developed a set of simulations dedicated to the understanding of issues related to the imaging of geostationary objects with optical interferometers Ref. 1–7. Here we use these simulations to investigate two issues related to this problem, the sampling density of the array and how the target size relative to the size of the telescope influences the observed visibility amplitude and throughput.

2. NUMBER OF TELESCOPE POINTINGS

The simulations presented here follow the ones presented in Ref. 5, which were created using the software package AIPS 8. For the first set of comparisons we use a high resolution model of a satellite over which we superposed bright fiducial targets separated by 10, 12 and 14cm along different directions (Fig. 1). The target is assumed to be at an altitude of 37,000 km. The simulations assume that the observations are done at the wavelength range 550nm to 1μm, split over 100 channels of equal wavenumber. We assume a central telescope and movable telescopes located at rings of 2.3, 4.2, 7.6, 13.7, 25, 45.4, 82.5 and 150m. The radius of these rings and spectral resolution are selected in order to have $Q_S \sim 2$ in the radial direction. We simulated observations with azimuthal sampling of the uv-plane in the range $0.15 \leq Q_S \leq 2$. The number of telescope positions at each ring is given by $N_B = (\pi B/\lambda_{max}) Q_S \theta_{max}$, where λ_{max} is the longest wavelength, θ_{max} is the largest angular extent of the target (assuming a maximum dimension of 15 m), and B is the baseline length. For the case of $Q_S = 1$ we need 4, 7, 12, 22, 39, 71, 128 and 232 positions for the different rings (smaller to larger).

Further author information: (Send correspondence to H.R.S.)E-mail: hschmitt@ccs.nrl.navy.mil, Telephone: 1 202 767 2977

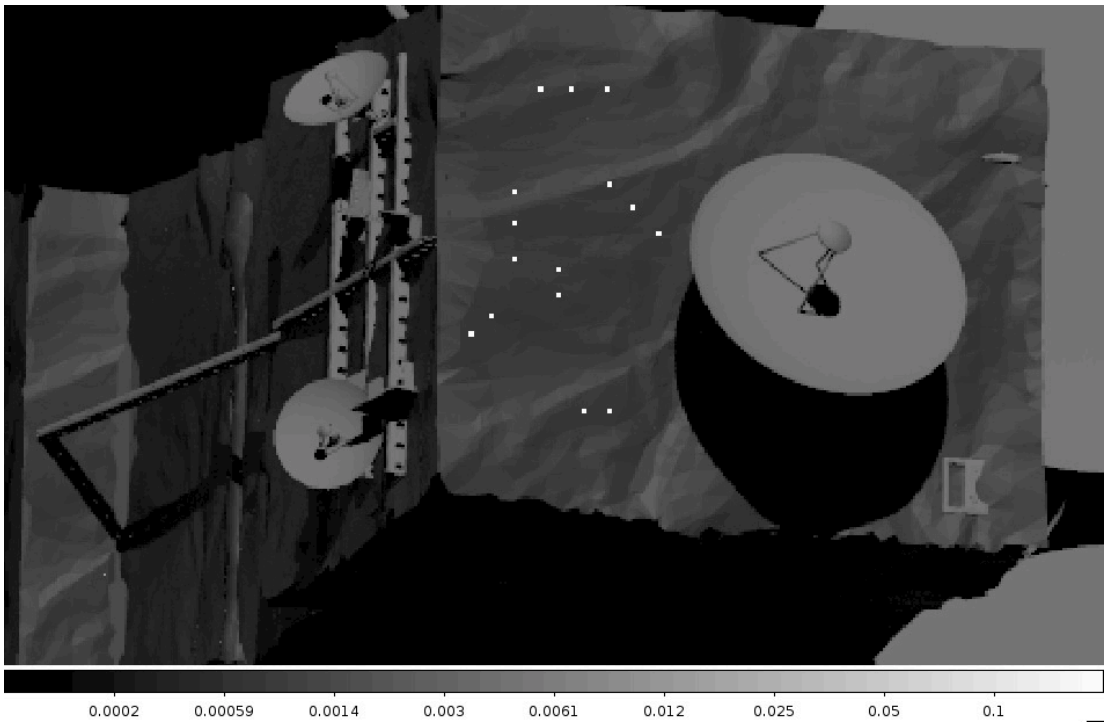

Figure 1. View of the satellite bus and the fiducial targets. The triple targets are separated by 12 and 14 cm, while the double targets are separated by 10 cm.

The simulated interferometric observations were used to synthesize images of the satellite. Fig. 2 shows the image obtained using $Q_S = 0.5$ sampling of the uv-plane. A visual inspection of the image indicates that we can resolve several details, as well as several of the fiducial pairs. The blotchy appearance of the image is due to the use of the Clean algorithm for the image deconvolution. Different image reconstruction algorithms, such a MEM, can minimize this effect. In Fig. 3 we show the cross section of the image reconstruction beams for a range of uv-plane density sampling cases. We find that there is virtually no difference between $Q_S = 1$ and 2. The FWHM of the beams do not vary significantly if one reduces the sampling to $Q_S = 0.5$. However, when moving from $Q_S = 0.5$ to lower values, we notice that the FWHM increases and the wings of the point spread function also become more prominent, which will in effect degrade the resolution of the image.

The image in Fig. 2 was also used to determine the resolution that can be achieved with these observations. By taking cross sections along the different pairs of fiducials (Fig. 4,5) we find that this image can spatially resolve fiducials separated by 12 cm, thus one needs a maximum baseline length of 185 m in order to reach a resolution of 10 cm.

3. TARGET SIZE AND TELESCOPE RESOLUTION

The second issue investigated in this paper is the the effects of telescope resolution on the observations of geosats. If one uses optical fibers to transport the light from the telescopes to the beam combiner, the coupling of the light from the telescope into the fiber can be represented by a gaussian corresponding to the resolution of the telescope. In Fig. 6 the left panel shows the model image of a geosat and the gaussian corresponding to a 1.5m

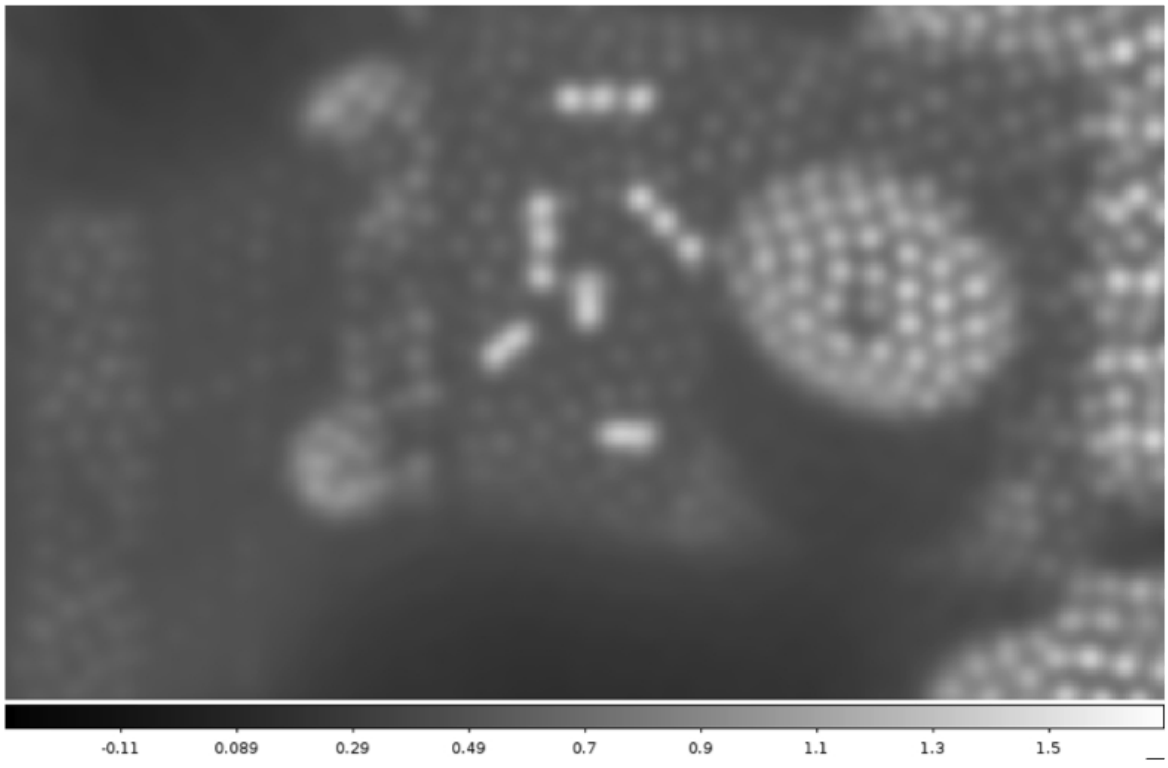

Figure 2. Synthesized image obtained with uv-plane azimuthal sampling of $Q_S = 0.5$.

telescope resolution at 550 nm. By convolving the image on the left with the corresponding gaussians at 1μm and 550 nm (bottom left and right panels, respectively), we see how much light from different parts of the target are coupled into the fiber. We find that a fair amount of light can be lost, especially at short wavelengths. This will reduce the number of photons being detected, in particular at short wavelengths.

In Figs. 7,8 we compare the visibility amplitudes at 1μm (red) and 550nm (black) for baselines along the E-W and N-S directions. We find that there is a slight increase in the visibility amplitudes at short wavelengths, with the strongest effect seen on baselines positioned along the longest dimension. The overall effect will be a reduction in the sensitivity of the system at shorter wavelengths.

4. DELAY COMPENSATION

In order to detect fringes it is necessary to compensate the extra delay path between different telescopes. This extra delay corresponds to three different components: internal delay, vacuum delay, and differential air path. Understanding, monitoring and controlling these variations is important, especially if one tries to use measurements in one spectral band to control the delay at another band. Internal delay, corresponding to the path followed by the light after reflecting on the telescopes and going through the beam combiner can be monitored by laser metrology. The vacuum delay is due to the geometry of the array, including variations in the target position and drifts in the telescope positions. Most of these variations are slow varying in time. The air path difference corresponds to the variations in the amount of air in front of different telescopes, and varies on time scales of a few milli seconds.

We used NPOI observations to investigate a method to correct the latter 2 effects. By using NPOI observations of a star that was coherently integrated to correct for the fringe displacement relative to zero delay, we are left with a residual phase variation that is due to uncorrected vacuum and air delay. The residual phase variations can be represented by the expression $f=a+bX^2$. Fig 9 bottom left panel shows the variation of b as a function of measured delay residual between 2 delay lines (laser metrology delay after to subtraction of the diurnal motion).

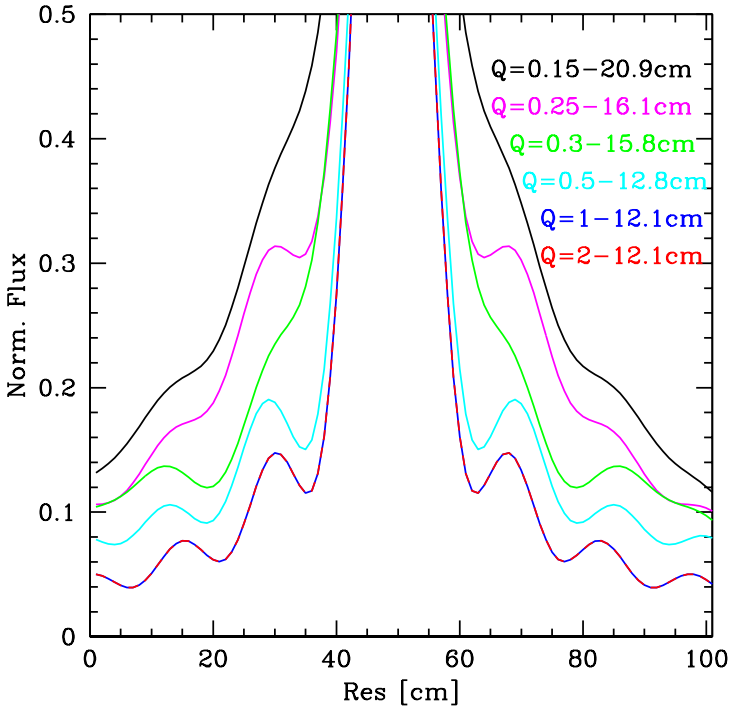

Figure 3. Comparison between the image reconstruction beams for different sampling of the uv-plane. The central region of the beams are fit with gaussians. The resulting full width half maximum for the different Q values are indicated in the figure.

We find that by adding a constant delay drift to the above delay, bottom right panel, we were able to reduce the scatter in the diagram. This delay drift is interpreted as a baseline error, which can be attributed to slow movements of the telescope over time. This technique shows that it is possible to correct for these 2 phase effects in post-processing, which reduces the control requirements and monitoring requirements of such a system.

ACKNOWLEDGMENTS

Basic research at the NLR is supported by 6.1 base funding.

REFERENCES

1. Jorgensen, A. M., Schmitt, H. R., Mozurkewich, D., Armstrong, J. T., Restaino, S., Hindsley, R. B. 2011, Advanced Maui, Optical and Space Surveilance Technologies Conference
2. Jorgensen, A. M., Schmitt, H. R., Mozurkewich, D., Armstrong, J. T., Hindsley, R. B., Baines, E. K. 2012, Advanced Maui, Optical and Space Surveilance Technologies Conference
3. Mozurkewich, D., Armstrong, J. T., Hindsley, R. B., Jorgensen, A. M., Restaino, S. R., Schmitt, H. R. 2011, Advanced Maui, Optical and Space Surveilance Technologies Conference
4. Mozurkewich, D., Armstrong, J. T., Hindsley, R. B., Jorgensen, A. M., Restaino, S. R., Schmitt, H. R. 2011, SPIE Conference Series 8165A, p.81650X
5. Schmitt, H. R. Mozurkewich, D., Restaino, S. R., Armstrong, J. T., Baines, E. K., Hindsley, R. B., Jorgensen, A. M., SPIE Conference Series 8165A
6. Schmitt, H. R., Mozurkewich, D., Restaino, S. R., Armstrong, J. T., Baines, E. K., Hindsley, R. B., Jorgensen, A. M. 2011, Proceedings AMOS meeting, Wailea, Maui, Hawaii, September 13-16 2011, Eds. S. Ryan, p. E76

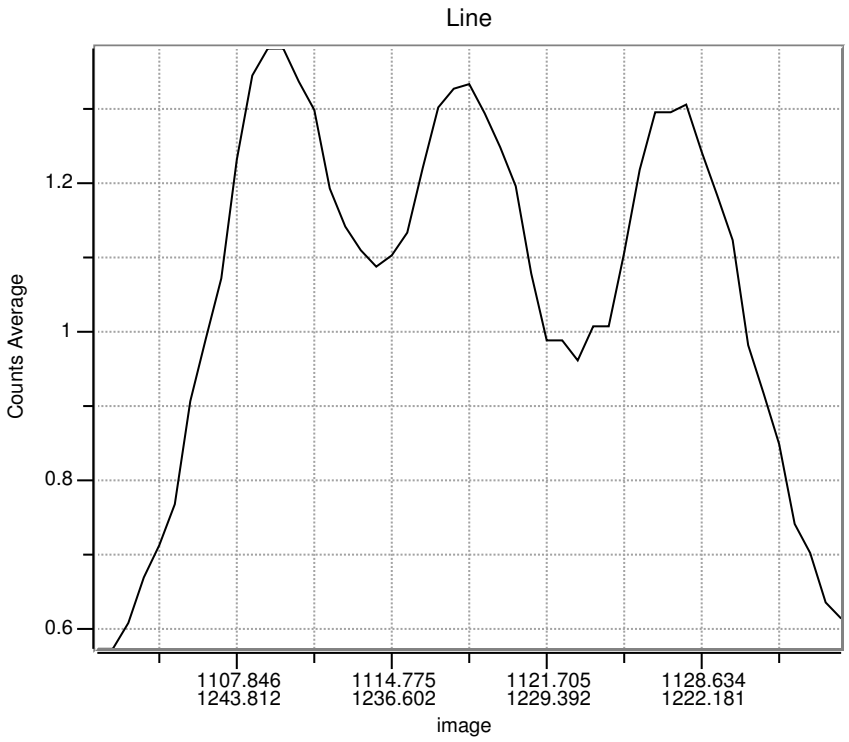

Figure 4. Cross section through a set of triple fiducials with a separation of 12 and 14 cm (left to right).

7. Schmitt, H. R., JOrgensen, A. M., Mozurkewich, D., Restaino, S. R., Armstrong, J. T., Baines, E. K., Hindsley, R. B. 2012, Advanced Maui, Optical and Space Surveilance Technologies Conference
8. van Moorsel, G., Kemball, A., Greisen, E., Astronomical Data Analysis Software and Systems V, Ed.s G. H. Jacoby & J. Barnes, Astronomical Society of the Pacific Conference Series, Volume 101, p. 37 (1996)

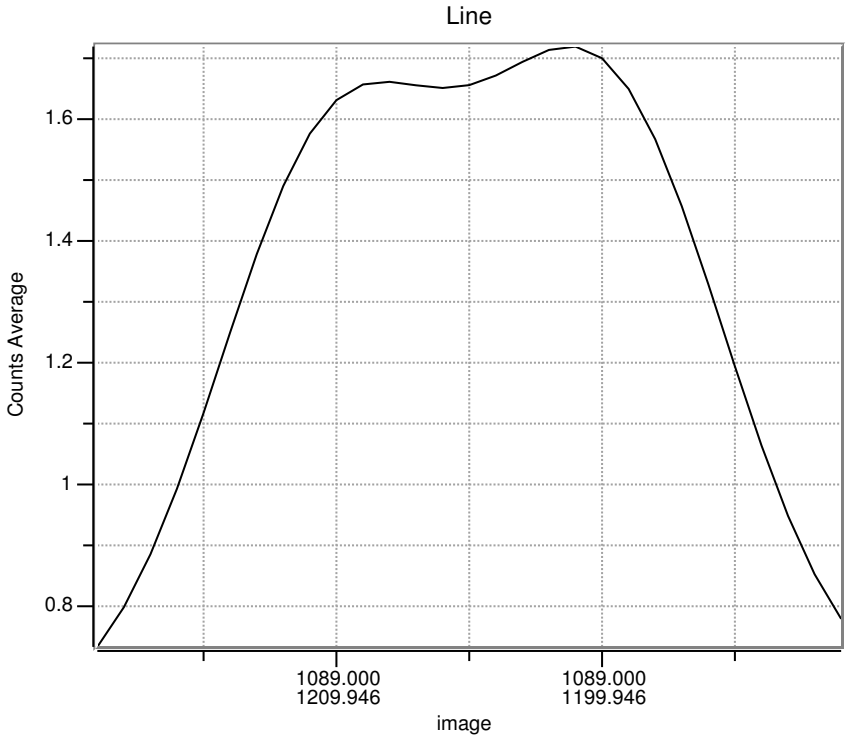

Figure 5. Cross section through a set of fiducials with a separation of 10 cm.

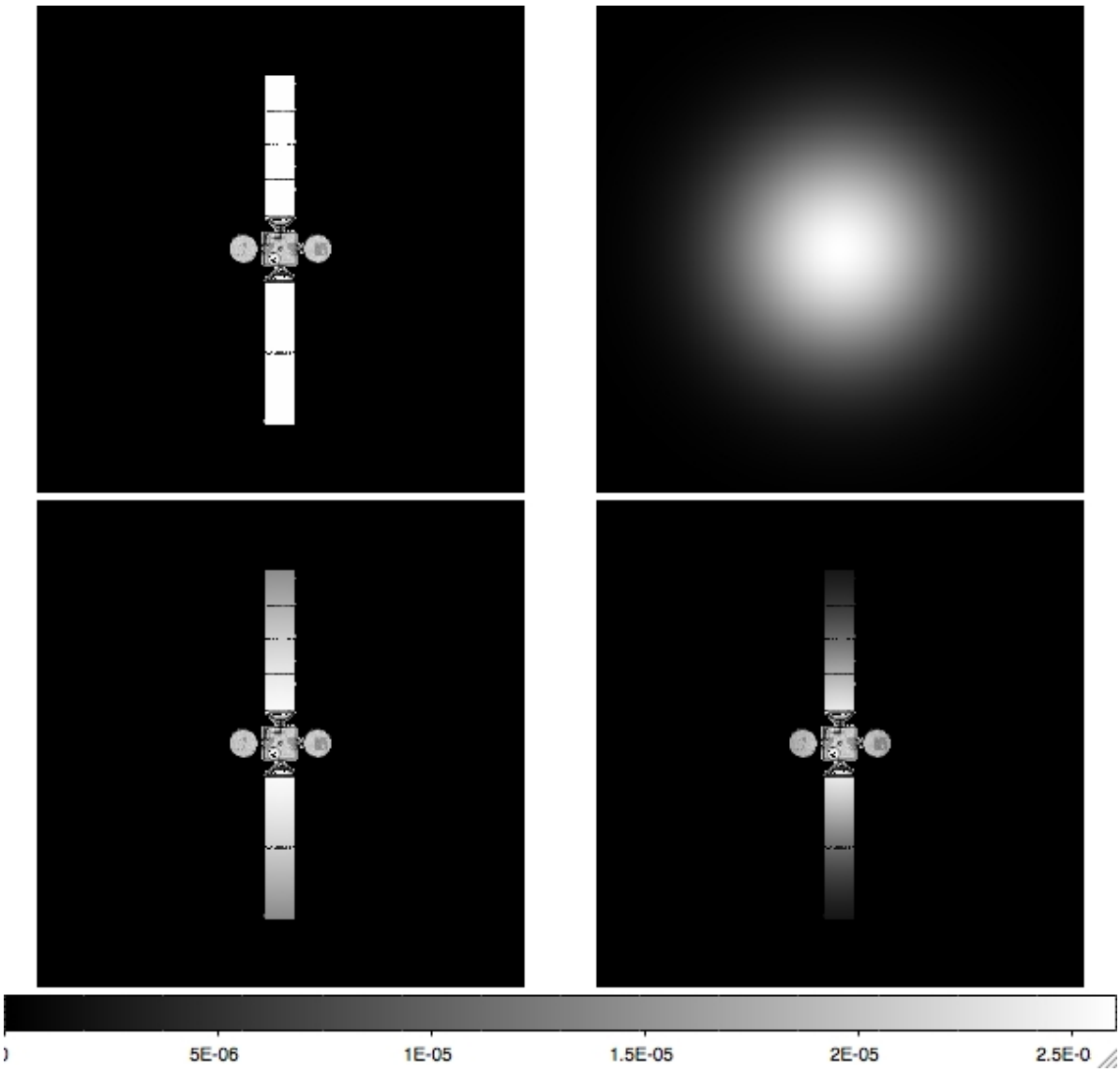

Figure 6. Effects of resolution on the amount of light coupled with a fiber.

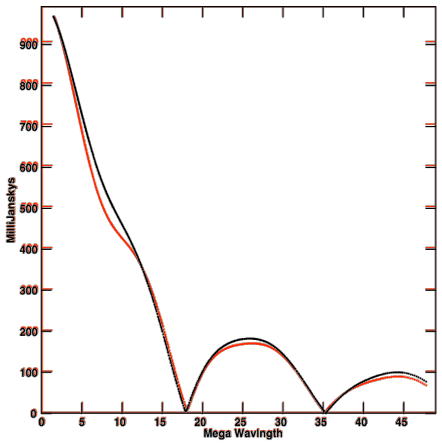

Figure 7. Visibility amplitudes along the E-W direction. Red is for 1μm, black is for 550 nm.

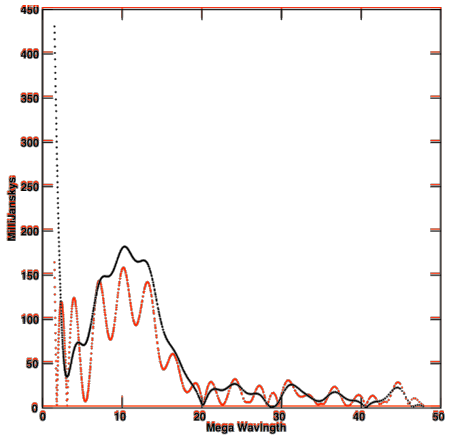

Figure 8. Visibility amplitudes along the N-S direction. Red is for 1μm, black is for 550 nm.

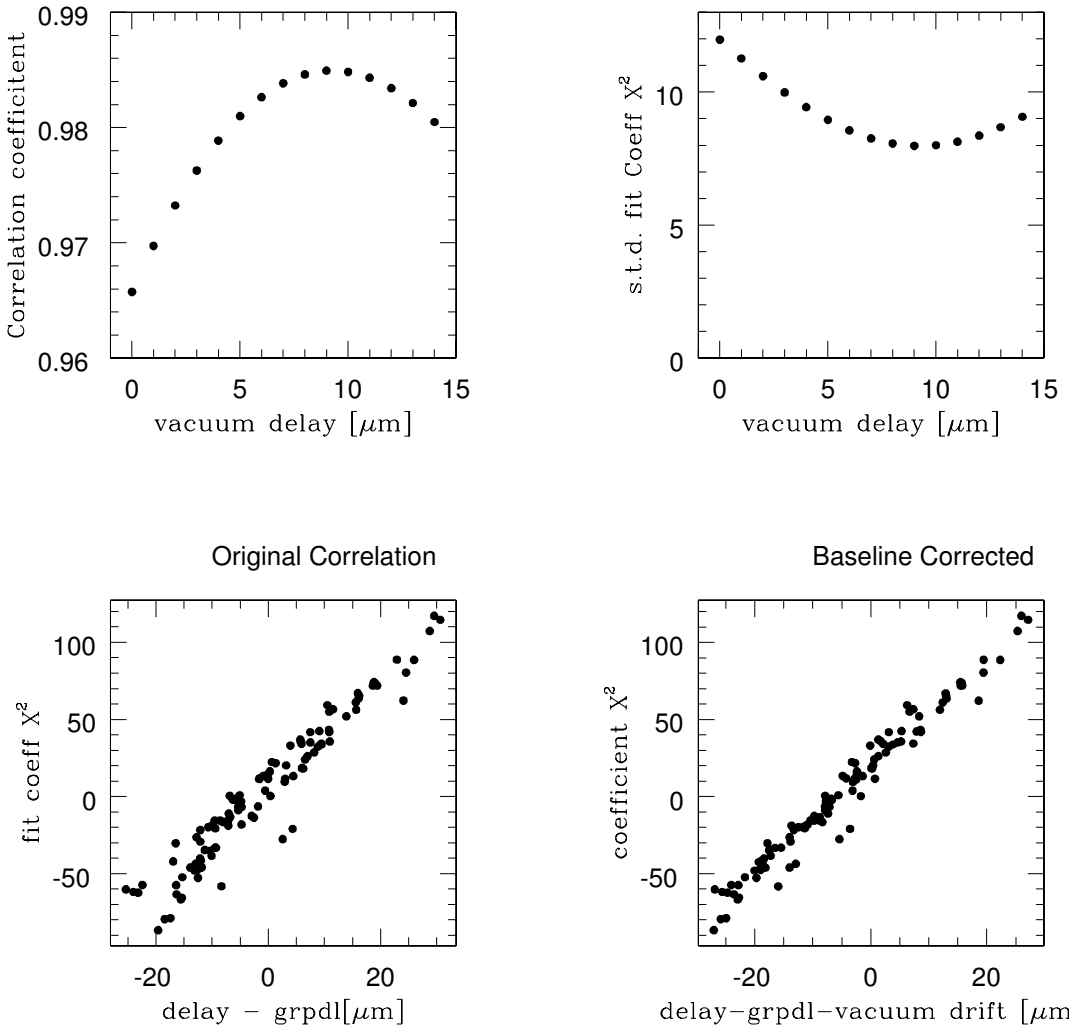

Figure 9. The top row shows the correlation coeficcient and χ^2 for different amounts of delay drift. The bottom left panel shows the original quadratic phase coefficient as a function of Fast Delay Line residual, while in the bottom right panel we show these numbers after removing a constant baseline drift rate.